ACS APPLIED NANO MATERIALS

www.acsanm.org

Article

Unified Understanding of Water Transport in Graphene Oxide-Modified Membranes for High-Flux and High-Selectivity Desalination Membranes

Yan A. S. da Campo, Ezequiel Lorenzett, Paulo A. Netz, Marcelo L. Pereira Junior, Claudia K. B. de Vasconcelos, Glaura G. Silva, Marcia C. Barbosa,* and Mateus H. Köhler*

Cite This: ACS Appl. Nano Mater. 2026, 9, 7994−8008

Read Online

ACCESS | Metrics & More | Article Recommendations | Supporting Information

ABSTRACT: Understanding the mechanisms governing water transport in graphene oxide (GO) membranes remains a central challenge in the development of next-generation desalination materials. In this work, commercial polyamide reverse osmosis membranes were coated with GO using an in situ dynamic pressurization method, followed by a comprehensive characterization and performance evaluation. Experimentally, GO deposition altered surface morphology, reduced roughness, and increased hydraulic permeability by ∼25% while maintaining salt rejection above 90%. Raman spectroscopy confirmed the incorporation of GO, and AFM and SEM revealed smoothing of the ridge-and-valley structure characteristic of interfacially polymerized polyamide layers. To elucidate the molecular origins of these changes, we performed a systematic series of molecular dynamics (MD) simulations that isolate the effects of slit width, interlayer spacing, and commensurability in stacked GO galleries. The simulations demonstrate that enhanced permeability is linked to the formation of low-friction pathways, reduced hydrogen-bond (HB) structuring, and the emergence of preferential flow routes within GO nanochannels. High commensurability between adjacent slits increases dynamic coupling and suppresses bottlenecks, while geometric expansion of the channels accelerates water mobility without compromising ion exclusion. By integrating experimental observations with molecular-scale analysis, this study provides a unified mechanistic picture of water transport in GO-modified membranes. The synergy between surface smoothing, nanoscale alignment, and reduced interfacial friction explains the observed enhanced permeance and highlights how targeted control of GO morphology can be leveraged to optimize membrane performance. These findings establish a multiscale framework for the rational design of high-flux, high-selectivity desalination membranes based on graphene-derived materials.

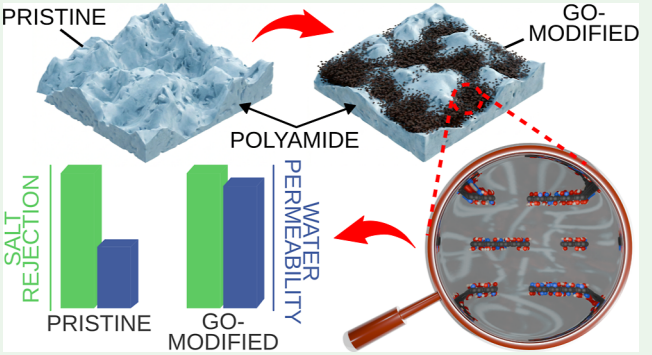

KEYWORDS: *desalination, membranes, reverse osmosis, graphene oxide, water, molecular dynamics*

1. INTRODUCTION

Water scarcity is one of the most significant challenges of our time.[1] To define whether there is water scarcity, one must consider the amount of freshwater available to meet a population's needs.[2] Currently, approximately half a billion people live with severe water scarcity on a year-round basis. At the same time, half of the global population is affected by severe water shortages for at least one month per year.[2] On top of that, of the total water on Earth, only 0.3% is freshwater readily available for human use. The remaining 99.7% is composed of 97% seawater and 2.7% freshwater stored in inaccessible locations, such as glaciers and deep aquifers. Water scarcity is a growing problem, driven by factors such as intense industrial use and rapid population growth.[3] This situation underscores the urgent need to adopt sustainable measures for managing water resources.

Effective approaches to combating water scarcity include improving water conservation systems, promoting water reuse and recycling, and increasing water-use efficiency across all major consumption sectors.[4] In practice, however, a more direct and increasingly common solution has been desalinating seawater, which provides a long-term water supply to help mitigate scarcity.[5]

Of the various desalination processes, reverse osmosis (RO) is the leading technology globally. This method utilizes a

Received: January 8, 2026
Revised: April 20, 2026
Accepted: April 21, 2026
Published: April 26, 2026

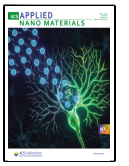

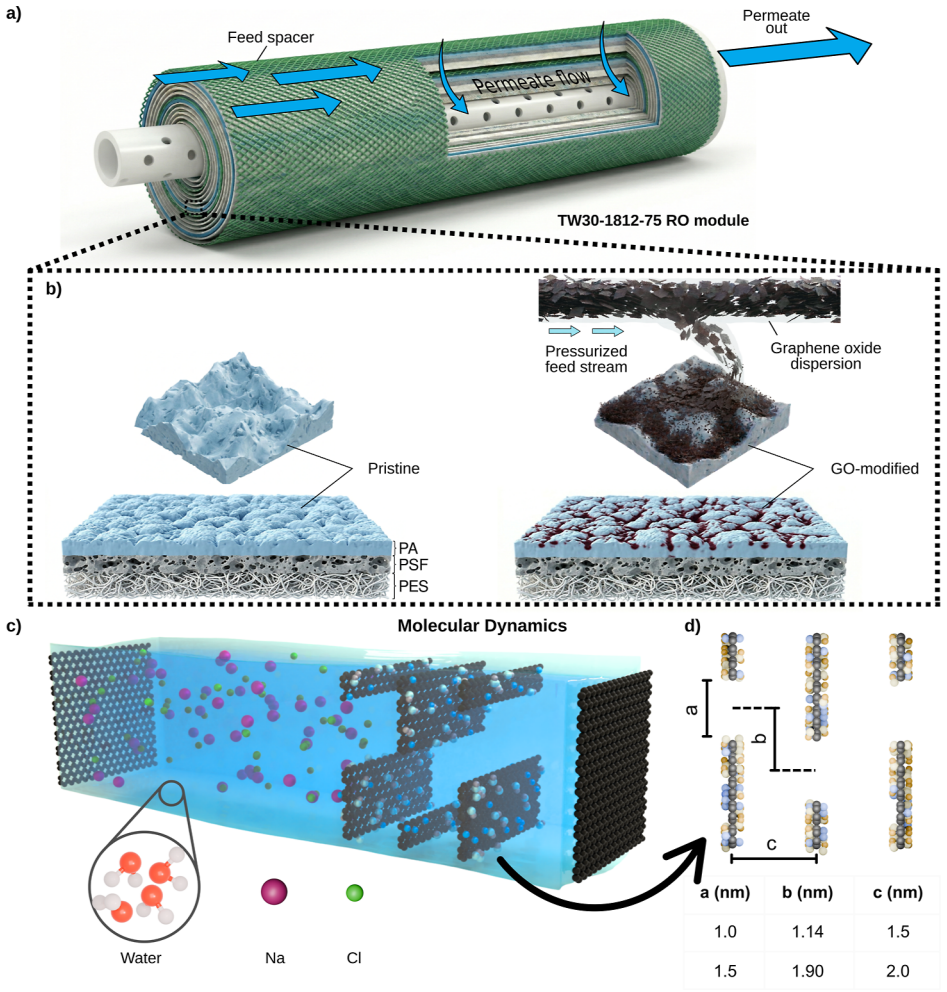

Figure 1. (a) Internal architecture of the RO module. (b) Surface modification process: cross-section and top-view of pristine PA (highlighting ridge-and-valley morphology) vs GO-modified PA (illustrating smoothing and GO accumulation). (c) Molecular dynamics framework showing the graphene piston pressing the aqueous NaCl solution against the GO membranes, and (d) the definitions of geometric parameters used in the simulations.

semipermeable membrane that selectively transports ions between two reservoirs. In natural osmosis, water flows from a region of lower solute concentration to a region of higher concentration to achieve osmotic equilibrium. This process creates an osmotic pressure. To reverse this natural flow and thus achieve desalination, an external pressure must be applied to the more concentrated (saline) side. When this applied pressure exceeds the osmotic pressure, the water molecules are forced through the membrane, leaving the ions behind and effectively separating freshwater from the saline solution.

Currently, the most widely commercialized membranes are spiral-wound modules composed of ultrathin polyamide (PA) layers formed via in situ interfacial polymerization atop a microporous polysulfone (PSF) support and a polyester (PES) base.[6] The ultrathin PA layer provides adequate water permeability, high salt rejection, and operational stability across a broad pH range. However, several limitations have been identified in these systems. Notably, PA is susceptible to oxidative degradation by chlorine, which compromises the integrity of the selective layer.[7] Furthermore, biofouling, primarily due to the accumulation of microorganisms, reduces membrane lifespan and results in significant losses in desalination performance.

Additionally, it is essential to note that polymeric membrane-based desalination technologies are approaching the thermodynamic efficiency limit, suggesting that further performance improvements may be marginal.

Carbon-based nanomaterials have been extensively investigated as filtration media due to their high selectivity and exceptional water permeability.[8−10] They also offer the possibility of surface functionalization through the incorporation of functional groups such as hydroxyl, carboxyl, epoxy, and amine, which can further enhance specific properties, as in the case of graphene oxide (GO).[11] In principle, the use of such nanomaterials is not intended to replace conventional polymeric membranes immediately, but rather to be integrated into existing membrane systems to improve performance, as exemplified by polyamide−graphene oxide (PA−GO) composite membranes.[12]

Molecular dynamics (MD) simulations have demonstrated that, compared to conventional polymeric membranes, membranes incorporating two-dimensional materials exhibit water fluxes that are 2 to 3 orders of magnitude higher.[13] Atomistic studies on graphene oxide membranes have further shown that water transport depends strongly on nanoscale confinement, interfacial friction, and the complex microstructure formed by pristine and oxidized regions within GO

https://doi.org/10.1021/acsanm.6c00110
ACS Appl. Nano Mater. 2026, 9, 7994−8008

sheets.[14−16] This exceptional permeability is attributed to the nanoscale confinement of water, which enhances its mobility, whether through the narrow diameters of nanotubes or nanopores, or through the openings in nanoslits.[17]

The presence of pores or slits in nanomembranes induces water molecules to form an organized bound structure near the pore or slit, which facilitates fast mobility. This organization is structured such that, in the presence of multiple pores, water flow is additive,[18] not exhibiting the turbulence typically observed in pure polymeric structures. One crucial question here is whether we can find a combination of distances and placements between membranes and slits that optimizes water flow in a multilayer organization of graphene oxide membranes.

In order to answer that question, we need to recognize that ion filtration in nanostructured membranes can occur via two primary mechanisms: (i) interlayer spacing in stacked membrane structures, where water flows through the gaps between layers, or (ii) engineered nanopores that allow water to pass while selectively rejecting ions. In nanoporous membranes, the number, spacing, and geometry of pores can be tuned. For nanoslit-based membranes, key parameters include slit distance, size, and the commensurability between the slit dimensions and the solvated ions.

In this work, we test whether the water flow through slits in GO membranes is affected by the distance between the membranes and the alignment of the slits in each membrane. This study has applications to actual polyamide membranes covered with GO surfaces, in which the slits are the interlayer packing discontinuities. Systems consisting of saline water forced against adjacent graphene oxide membranes were simulated to replicate experimental conditions and provide atomistic insights into the impact of geometrical factors, such as commensurability and interlayer spacing, on desalination. Notably, the experimental results indicate a change in water flux with specific configurations, findings further confirmed by simulations that show the impact of commensurability, slit width, and interlayer spacing on optimizing water passage. On the other hand, experimental results confirm the theoretical prediction of a lower impact of these conditions on salt rejection. The paper is organized as follows. In Section 2, we introduce the experimental setup and computational details. In Section 3, we present and discuss our results on water permeation, structural and dynamical aspects, and salt rejection in each system. Finally, a summary of our results and the conclusions are shown in Section 4.

2. MATERIALS AND METHODS

This study combines experimental membrane characterization with MD simulations to investigate how graphene oxide membranes influence water and salt transport behavior across different length scales. The experimental procedures describe the preparation, coating, and testing of commercial RO modules, while the computational framework isolates the geometric parameters that control nanoscale water flow.

2.1. Experimental Setup

A GO dispersion was prepared at 100 mg·L^{-1} in a 50% v/v ethanol−water mixture and homogenized by sonication to promote a uniform distribution of the sheets. The pH of the dispersion was subsequently adjusted to 8.5 with a 0.1 mol·L^{-1} NaOH solution.

Commercial spiral RO modules (TW30-1812-75, active area 0.25 m^2) were modified in situ, without opening the elements, following a dynamic pressurization protocol from optimized procedures reported in the literature.[19] A schematic illustration of the internal architecture of the RO module is shown in Figure 1a. Before the modification step, each module was flushed with distilled water in recirculation mode for 30 min to remove preservatives and soluble residues. The GO dispersion was then circulated through the membrane module at 3.5 bar and a flow rate of 3.6 L·min^{-1} to prepare the modified membrane (GO-modified). To distinguish effects arising specifically from GO, control modules underwent the same pressurization and recirculation sequence using only the 50% v/v ethanol solution adjusted to pH 8.5 to prepare unmodified or pristine membranes. The cross-section of pristine PA and the transition from a highly irregular topography to a smoother surface are schematically illustrated in Figure 1b. While the pristine PA layer exhibits a pronounced ridge-and-valley morphology—a direct result of the interfacial polymerization process—the subsequent GO modification levels these features.

Raman spectroscopy was used to characterize the chemical structure of the modified membranes. Measurements were performed on a WITec Alpha 300R confocal Raman system equipped with a 457 nm excitation laser (1−3 mW), acquiring five spectra at different locations on each sample at 20 °C. Surface morphology and nanometric features were examined by scanning electron microscopy (SEM, FEI Quanta 3D FEG) and atomic force microscopy (AFM, Cypher ES).

Membrane performance was evaluated both before and after GO treatment. Hydraulic permeability and salt rejection measurements were performed using three different membranes under each condition. Before testing, the spiral-wound elements were compacted with deionized water at 6 bar until a stable permeate flow was reached, after which hydraulic permeability and salt rejection experiments were conducted. Hydraulic permeability was determined by operating the system at pressures from 2 to 6 bar, keeping the feed flow rate constant at 2.4 L·min^{-1} with distilled water. The feed temperature was controlled at 25 ± 2 °C using a recirculating chiller. Permeate flow was recorded at each operating condition and normalized to 25 °C. The permeability coefficient (P) was obtained from the slope of the permeate flux versus applied pressure.[20] To account for intrinsic variability among commercial RO elements, the relative permeability (P/P_0) was calculated as the ratio between the permeability after modification and the initial permeability.

Salt rejection experiments were performed using a 2.0 g·L^{-1} NaCl feed solution at 3.5 bar and 2.4 L·min^{-1}. Rejection (R) was determined from the conductivity difference between feed and permeate streams following established procedures.[21]

2.2. Molecular Dynamics Details

Classical MD simulations were performed using the large-scale atomic/molecular massively parallel simulator (LAMMPS).[22] The simulations and data analysis focus on the impact of introducing GO membranes, highlighting geometrical, physical, and chemical aspects. The systems were built with three adjacent GO layers placed between two reservoirs, as shown in Figure 1c: a feed reservoir, with all salt concentration, and a permeate reservoir. In the simulations, we adopted a salt concentration of approximately 0.5 M, slightly below seawater levels, to ensure sufficient ion density for the convergence of transport and interaction properties.[23,24] The number of molecules in the left reservoir was the same at the beginning for all systems. The sheets had an oxidation degree of 20%, with functional groups distributed as 2/3 hydroxyl (OH) and 1/3 epoxy (O). Graphene pistons were used as pressure controllers. Additionally, two different values of slit size (1.0 and 1.5 nm), intersheet distance (1.5 and 2.0 nm), and commensurability (high and low) were tested to evaluate the effect of geometric parameters on water flow behavior and salt rejection. Commensurability indicates how well two adjacent slits are aligned. Therefore, smaller values of b correspond to higher commensurability, as illustrated in Figure 1d. The parameter b was set to 1.14 and 1.9 nm, corresponding to 50% and 70% spacing between the midlines of adjacent slits, relative to the total sheet height. The cross-sectional area of the systems is 14.82 nm^2. In Table 1, we present the eight systems identified from GO1 to GO8 according to their geometric properties, including slit size, interlayer spacing, and degree of commensurability.

https://doi.org/10.1021/acsanm.6c00110
ACS Appl. Nano Mater. 2026, 9, 7994−8008

Table 1. Configurations Showing Slit Size, Interlayer Spacing, and Commensurability

system	slit size (nm)	interlayer spacing (nm)	commensurability
GO1	1.0	1.5	low
GO2	1.0	1.5	high
GO3	1.0	2.0	low
GO4	1.0	2.0	high
GO5	1.5	1.5	low
GO6	1.5	1.5	high
GO7	1.5	2.0	low
GO8	1.5	2.0	high

In each simulation, the systems were first relaxed by a 1 ns energy minimization step performed in the *NVT* ensemble (constant number of particles, volume, and temperature). After minimization, an *NPT* ensemble (constant number of particles, pressure, and temperature) was applied by compressing the pistons until the water density stabilized around 1 g/cm^3. Then, a new *NVT* ensemble was used to equilibrate the system at the latest volume for 1 ns. Finally, an *NPT* ensemble was applied to create a nonequilibrium regime by unidirectionally pushing the pistons with a pressure gradient of 3000 bar until the spacing between the piston and the first layer reached 2 nm. Data were collected during this final stage. Although the 3000 bar pressure gradient is orders of magnitude higher than the experimental conditions (3−6 bar), this approach is a well-established acceleration protocol that preserves the consistency of transport mechanisms and selectivity trends reported at lower pressures.[25,26] We used the SPC/E[27] water model and constrained the molecules with the SHAKE algorithm.[28] The time step was set to 0.5 fs, and the temperature was set to 300 K using a Nosé−Hoover thermostat[29] with a damping time of 100 fs. The graphene oxide sheets were kept rigid, a protocol planned to isolate the effect of varying each geometrical parameter on water transport through the membrane. The Lennard-Jones interaction parameters and atomic charges used in the simulations are listed in Table S1 of the Supporting Information. The particle−particle particle-mesh (PPPM) method was used to compute long-range electrostatic interactions beyond a 1.2 nm cutoff.

3. RESULTS AND DISCUSSION

Water transport through GO-modified membranes emerges from the interplay between surface organization, nanoscale confinement, and the chemical landscape imposed by GO. The following results highlight how these elements shape the movement of water and ions, revealing the conditions under which GO promotes enhanced flow while preserving selective transport.

Our assumption is that the decrease in friction allows water to be more mobile, which is facilitated by the organization of water molecules as they approach the nanoslit due to the hydrogen-bond (HB) network and the smooth nature of the GO surface. This hypothesis is tested here using experiments and simulations.

3.1. Pristine and GO Membranes: Experimental Results on Water and Salt Structure and Mobility

The pristine membrane, shown in Figure 2a, exhibits a light and uniform surface with no visible markings or grooves. In contrast, the GO-modified is shown in Figure 2b, displaying a pronounced change in appearance: well-defined grooves emerge across the surface, matching the geometry of the

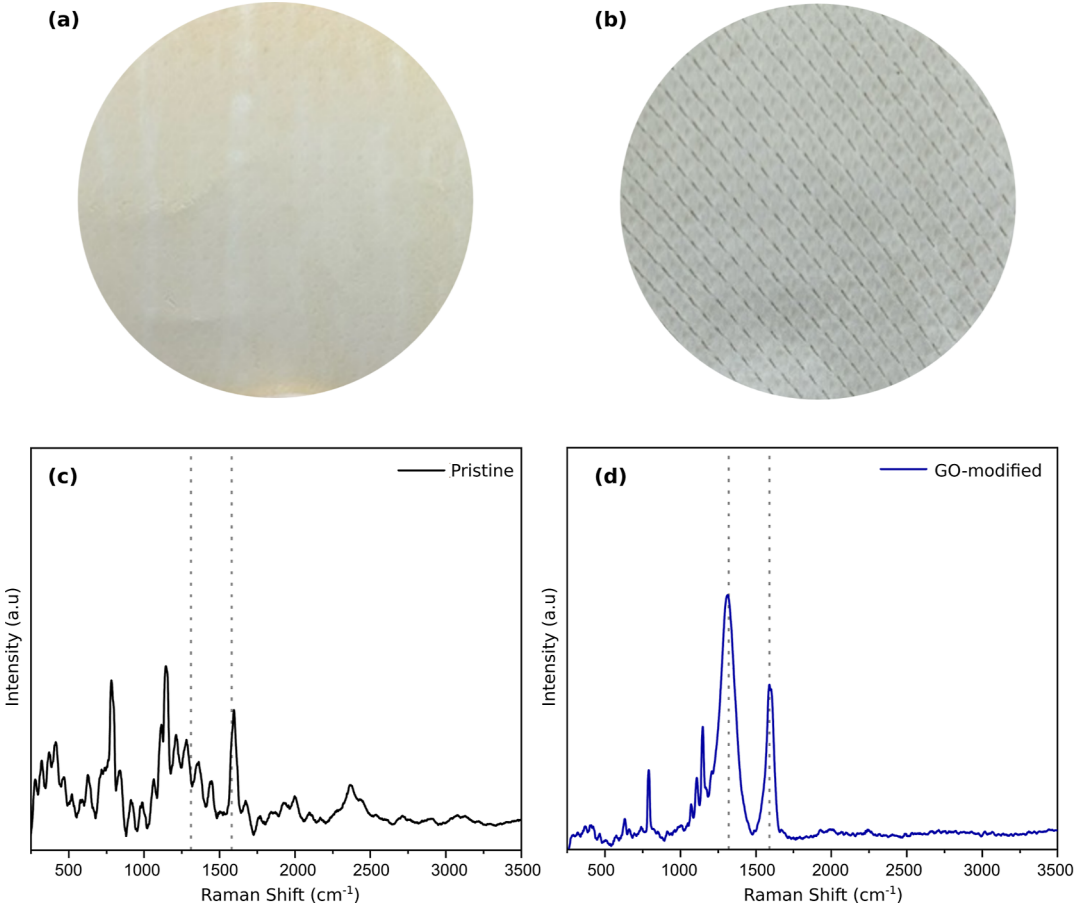

Figure 2. Optical microscopy images (16× magnification) and Raman spectra of the membranes (a,c) pristine and (b,d) GO-modified membranes.

https://doi.org/10.1021/acsanm.6c00110
ACS Appl. Nano Mater. 2026, 9, 7994−8008

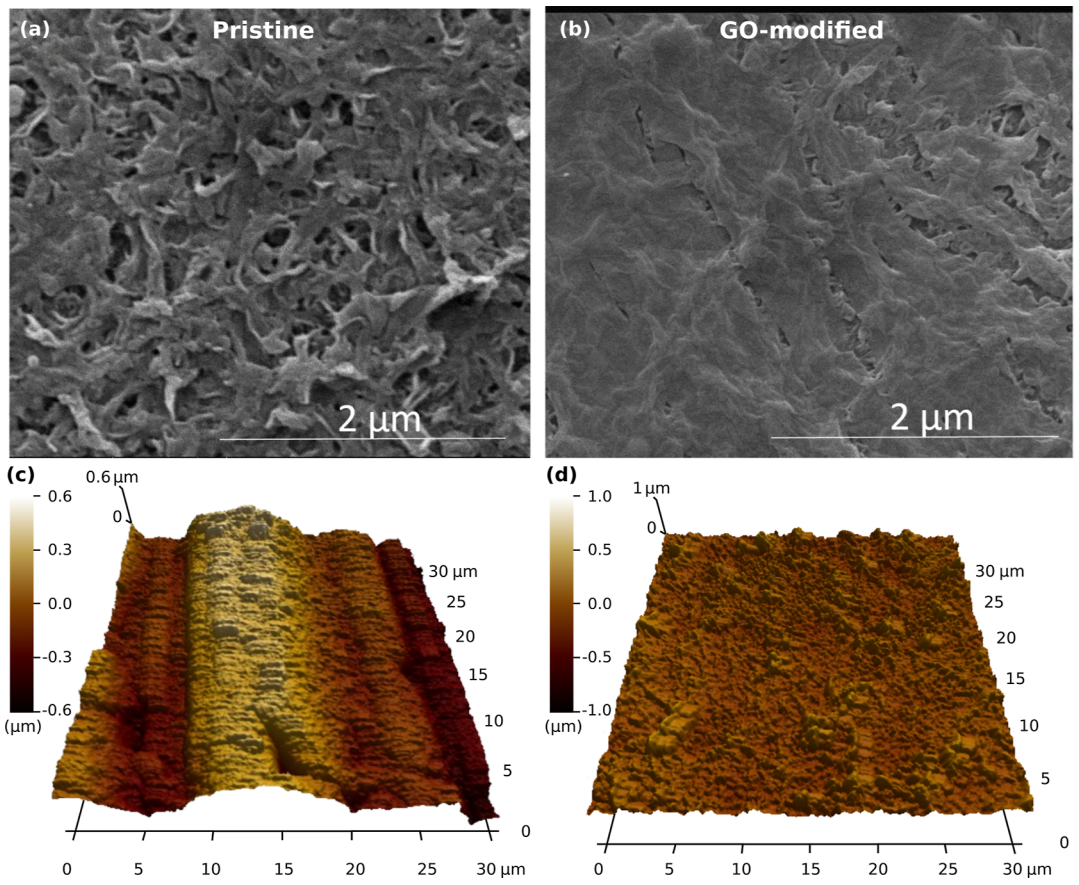

Figure 3. Scanning electron microscopy images of (a) the pristine and (b) the GO-modified membranes. Surface topography obtained by atomic force microscopy for (c) unmodified and (d) modified membranes.

polymeric mesh used as the feed spacer in spiral-wound modules. Feed spacers play a crucial role in the performance of RO systems. Besides providing mechanical support and minimizing pressure drop, they create flow channels, reduce concentration polarization, and introduce controlled microturbulence that helps mitigate fouling and biofouling. The brownish coloration observed along the grooves of the GO-modified membrane suggests preferential deposition or accumulation of GO in these regions. This indicates that the transport and distribution of the modification dispersion inside the module are strongly influenced by the presence of the spacer, which directs the flow paths and locally enhances GO retention.

The presence of GO on the membrane surface is further supported by the Raman spectra shown in Figure 2c,d. Two Raman shifts widely recognized as key identifiers of GO are highlighted by the vertical dashed lines in the spectra. The peak at ∼1360 cm^{-1} corresponds to the D band, which is associated with structural defects introduced by oxygen-containing functional groups such as epoxy, carbonyl, and hydroxyl groups. These disruptions in the sp^2-hybridized C−C network are characteristic of the oxidized and defect-rich structure of graphene oxide.[30] The G band, located near 1585 cm^{-1}, arises from the in-plane vibrational modes of sp^2-bonded carbon atoms and reflects the remaining ordered graphitic domains. The simultaneous appearance of both D and G bands in the modified membrane constitutes clear evidence of GO incorporation into the polymeric surface. In contrast, their absence in the pristine membrane confirms the lack of carbon-based nanomaterial prior to modification.

In addition to the GO-related bands, characteristic vibrational features of the underlying membrane materials are also observed in all spectra. For the PA selective layer, bands appear at 634 cm^{-1} (CN vibration), at 1070 and 1109 cm^{-1} (C−C stretching), and at 1600−1608 cm^{-1} (amide group vibrations), consistent with previous reports.[31] Signals originating from the polysulfone (PSF) support layer are likewise present, including the distinctive band at 791 cm^{-1} attributed to Ar−S−Ar stretching and an additional peak at 1149 cm^{-1} corresponding to the symmetric stretching of the sulfone (SO_2) group.[32] The persistence of these PA and PSF features across all samples indicates that the GO deposition process does not alter the chemical structure of the base membrane. In contrast, the emergence of the D and G bands uniquely in the modified membrane confirms the successful incorporation of GO.

The SEM image of the pristine membrane (Figure 3a) reveals a rough, nodular surface typical of polyamide dense layers formed via interfacial polymerization. These irregular structures are known to play a central role in water transport and solute rejection, as they define the selective morphology responsible for the membrane's performance in aqueous separation processes.[33] After the GO deposition, the surface morphology changes noticeably. As shown in Figure 3b, the GO coating smooths out part of the irregularities observed in the unmodified membrane. This attenuation of the nodular features is consistent with previous reports on GO-modified polyamide membranes, where the incorporation of GO

https://doi.org/10.1021/acsanm.6c00110
ACS Appl. Nano Mater. 2026, 9, 7994−8008

increased surface hydrophilicity and introduced antifouling characteristics.[33−35]

Atomic force microscopy (AFM) images obtained in noncontact mode are presented in Figure 3c,d, enabling a detailed analysis of surface topography and roughness. Polyamide membranes used in reverse osmosis typically exhibit a ridge-and-valley morphology, as shown in the pristine sample. The GO-coated membrane exhibits reduced height variation compared to the unmodified membrane, resulting in significantly lower roughness metrics, including maximum height, minimum height, root-mean-square roughness (R_q), and average roughness (R_a), as summarized in Table 2. The

Table 2. Surface Roughness Parameters Obtained from AFM Analysis Based on 786,432 Data Points[b]

AFM parameters[a]	pristine	GO-modified
R_a (nm)	200 ± 97	0 ± 0
R_q (nm)	283 ± 107	114 ± 80
R_{max} (nm)	990	637
R_{min} (nm)	−1248	−580

[a]N = 786,432. [b]The errors are the standard deviations among data points.

parameter N = 786,432 corresponds to the total number of data points (pixels) acquired and analyzed in a single surface scan, for a sampled area. One of the main effects of incorporating GO onto the membrane surface is altering its surface roughness profile.

One of the main effects of incorporating GO onto the membrane surface is altering its surface roughness profile. Previous studies have shown that the lamellar structure of GO enables it to occupy and level the valleys present on PA surfaces preferentially, leading to a pronounced reduction in roughness-related parameters.[36,37] This filling effect produces a smoother, more uniform topography, as confirmed by AFM and optical profilometry analyses. The combined SEM and AFM results indicate the presence of multiple overlapping GO sheets on the polyamide surface; considering the nanometric thickness of individual GO layers, this morphology strongly suggests the formation of intersheet nanochannels, which may act as preferential low-friction pathways for water transport. For the GO-modified membrane, the average roughness (R_a) decreased to zero, the lowest among all membranes evaluated. In addition, both the maximum and minimum roughness values were reduced, reinforcing the smoothing effect of GO deposition on the membrane surface.

Figure 4 presents the relative hydraulic permeability and salt rejection values for the pristine and GO-modified membranes. As expected, the salt rejection remained above 90% even after surface modification, indicating that the GO coating did not compromise the integrity of the selective polyamide layer. It is worth noting that, according to the membrane manufacturer, the typical NaCl rejection for these commercial spiral-wound elements exceeds 90% within the 2−4 g·L^{-1} concentration range; thus, the feed concentration adopted in this study (2.0 g·L^{-1}) falls within the recommended brackish-water operating window, and the measured rejection values are consistent with manufacturer specifications. In contrast, the hydraulic permeability increased by approximately 25% after GO deposition.

This enhancement is consistent with the widely discussed "frictionless channel" mechanism. According to this model, the hydrophilic edges and defect sites of GO nanosheets serve as

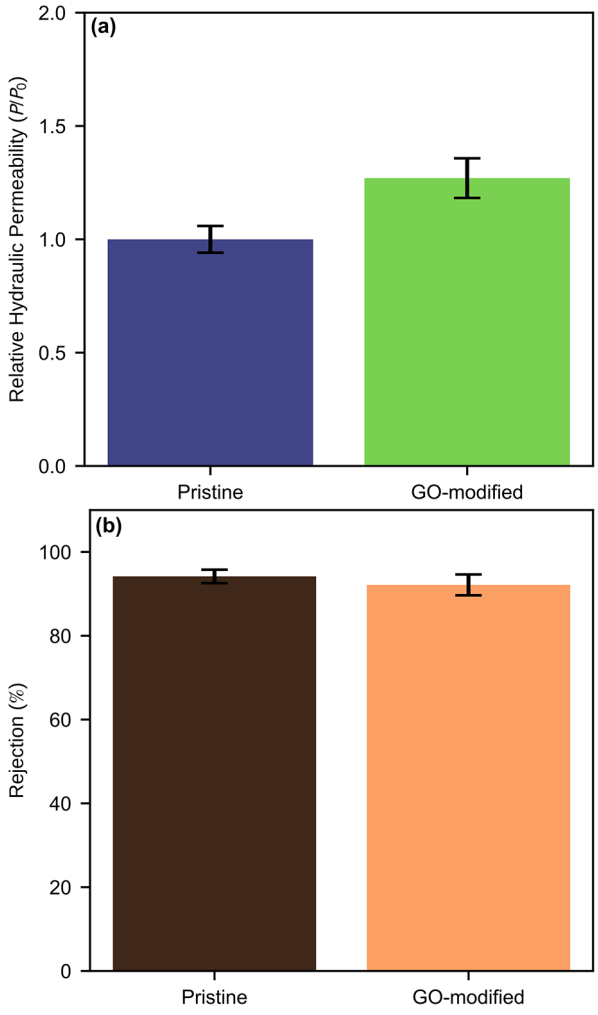

Figure 4. (a) Relative hydraulic permeability and (b) salt rejection for the pristine and GO-modified membranes. The averages were obtained from three independent tests, and the error bars represent their respective standard deviations.

entry points for water molecules. Once hydrated, molecules pass through these gate regions and move with increased mobility within the carbon-based nanocapillaries formed between adjacent GO sheets. The high water velocity is attributed to the extremely low friction at the water−graphitic interface, a phenomenon often referred to as drag-reduction or slip-flow behavior.[38]

Similar permeability enhancements have been reported by Bhoje et al.[39] who observed increases of comparable magnitude in thin-film composite reverse osmosis membranes modified with GO. Liu and Xu also reported that incorporating GO nanosheets onto polyamide surfaces led to sizable improvements in water flux within the same range, further supporting the mechanism proposed here.[12]

The experimental results presented thus far demonstrate that graphene oxide deposition significantly alters the membrane surface morphology and produces a marked enhancement in water flux without compromising salt rejection.

Although the literature proposes several plausible mechanisms, such as low-friction nanocapillaries and hydrophilic gate effects at the edges of GO nanosheets, none fully accounts for the superflow behavior observed in practice, and no consensus has yet been reached. To gain deeper insight into the

https://doi.org/10.1021/acsanm.6c00110
ACS Appl. Nano Mater. 2026, 9, 7994−8008

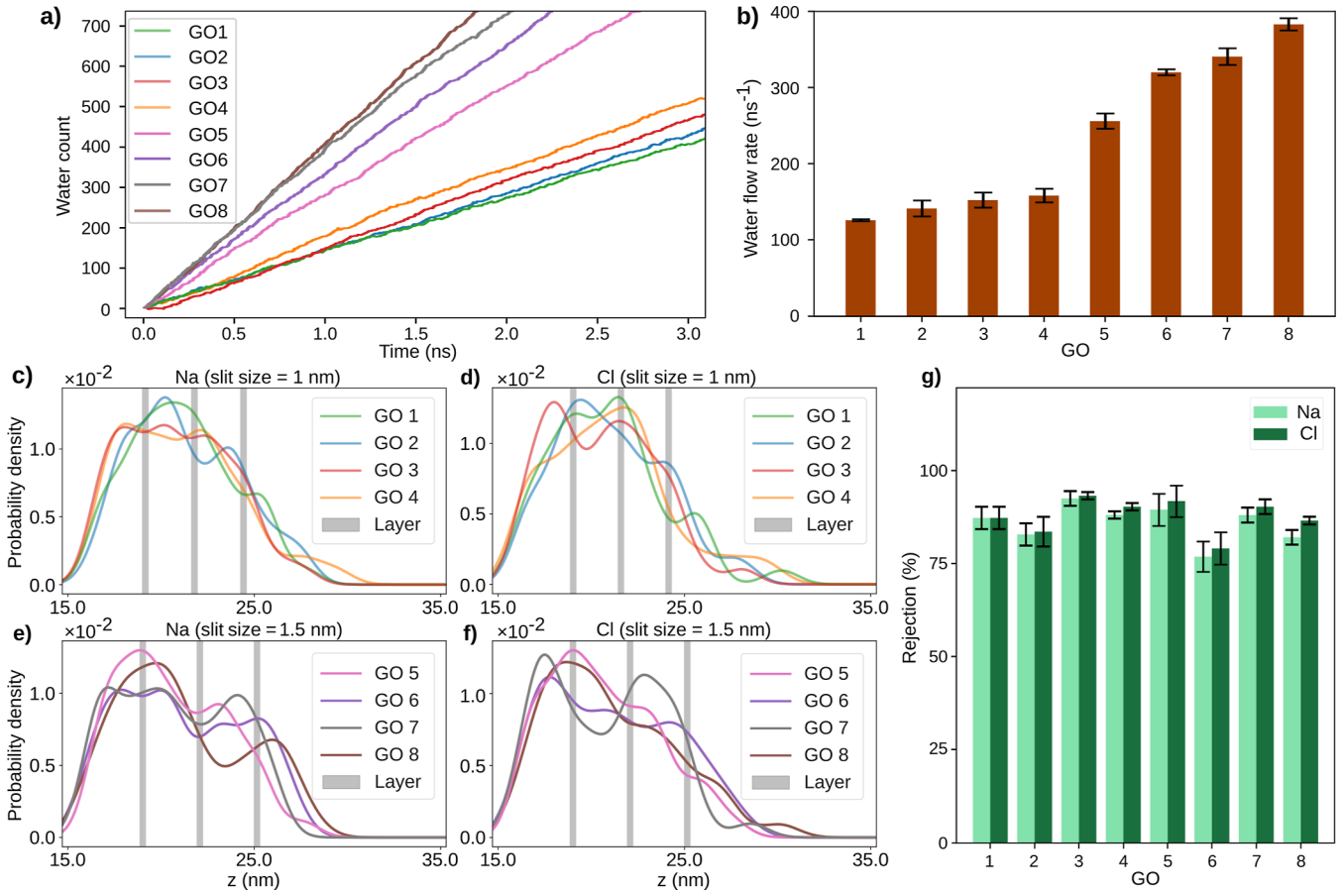

Figure 5. (a) Water accumulation in the permeate reservoir over time during the pressure-driven regime and (b) water flow rates for each system. (c–f) Averaged z-density profiles for sodium and chloride ions, with (g) ion rejection for each system. All data represent averages from five independent simulations.

molecular mechanisms governing this phenomenon and to isolate structural effects that cannot be directly probed in a spiral-wound module, the following section presents the theoretical analysis and molecular dynamics simulations developed for this study.

3.2. Simulation Results on Water and Salt Structure and Mobility in GO Membranes

In Figure 5 we show the water flow and salt rejection data from the MD simulations. Figure 5b shows that the slit size divides the system into two groups: a lower flow-rate group for 1.0 nm and a higher flow-rate group for 1.5 nm. A slight change in the slit aperture can cause a substantial increase in water permeation in these configurations. Indeed, previous studies have demonstrated that the opening size in a membrane is a decisive factor for water transport.[13,40]

The permeability shown in Figure 5b is a result of the linear fitting of the curves in Figure 5a, which depicts the water flow rate during the simulations and is divided into two groups with higher and lower passage of water molecules in time. The consequence can be visualized in Figure 5b, where we observe a strong difference in the permeability between systems with 1.0 and 1.5 nm slit sizes.

In the former, there is a very slight increase in the flow rate from the GO1 to the GO4 system (all averages still within the standard deviations). In contrast, in the latter, there is an apparent linear increase in the water flow rate from the GO5 to the GO8 system.

The increase in permeability observed here is associated with the other two geometrical factors investigated in this contribution: the interlayer spacing and the commensurability. Among the 1.0 nm slit size systems, those with a 2.0 nm interlayer spacing, GO3 and GO4 systems, exhibit higher permeability (while still within the standard deviation) compared to those with a 1.5 nm spacing, GO1 and GO2 systems. A similar tendency is observed for 1.5 nm slit systems. Each system with a fixed slit size and interlayer spacing has a corresponding pair with either low or high commensurability. Systems with higher commensurability (even-numbered systems) exhibit higher permeability compared to their counterparts with lower commensurability (odd-numbered systems).

In Figure 5c–f, we show salt distributions along the z-axis over the entire simulation time. Distinct behaviors are observed across all systems for both Na^+ and Cl^- species. The profiles exhibit peaks at different regions, suggesting possible nonlocal specificity in salt retention. More importantly, no preference for ion adsorption across the different geometries is observed, whereas all density profiles show similar occupation patterns and ion passage through the membranes.

The salt rejection (R) for each system, illustrated in Figure 5g, was obtained from the following equation

https://doi.org/10.1021/acsanm.6c00110
ACS Appl. Nano Mater. 2026, 9, 7994–8008

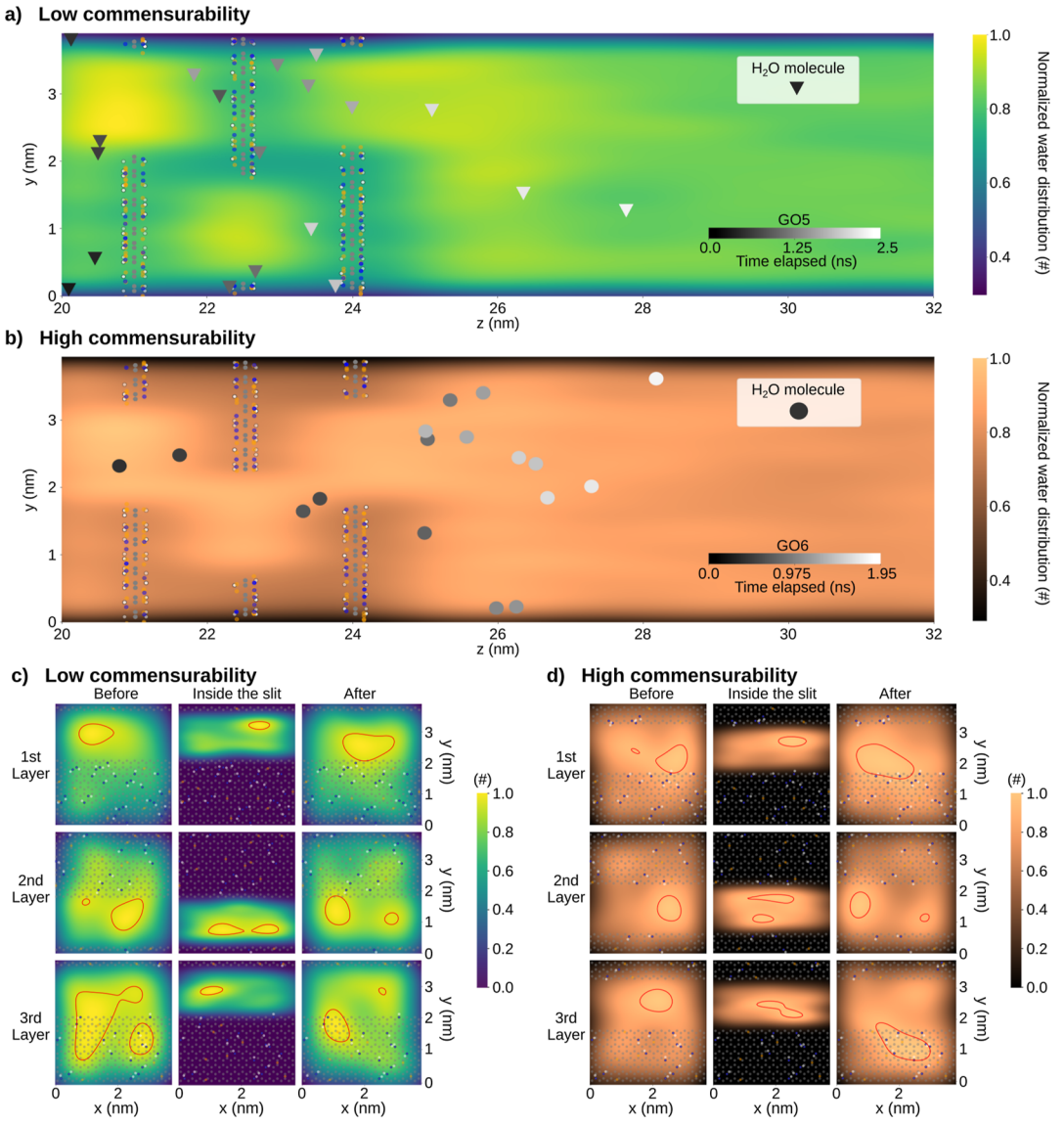

Figure 6. Lateral *z*-direction water distribution for (a) GO5 (low commensurability) and (b) GO6 (high commensurability), including tracked molecular trajectories. (c,d) Cross-sectional maps illustrating regions before, inside, and after the slits. Red contours delineate intensities exceeding 0.8.

$$R = \left(1 - \frac{C_i}{C_f}\right) \times 100 \tag{1}$$

where C_f is the salt ion concentration (Na^+ or Cl^-) in the feed reservoir and C_i is the concentration in the permeate reservoir.

In Figure 5g, we plot the salt rejection for the sodium and chloride for the eight cases. It reveals that variations in slit size and interlayer spacing do not lead to significant changes in salt retention for either Na^+ or Cl^- species, even though Cl^- has a larger hydration radius compared to Na^+.[41] However, subtle changes can be observed in systems with a larger slit size. Additionally, increasing commensurability results in a slight but consistent decrease in salt rejection across the systems, suggesting that creating a more tortuous pathway primarily hinders salt transport. Comparable permeability and salt rejection behaviors have been observed in previous studies of similar graphene oxide multilayer systems.[15,42,43] The most significant difference is observed between the GO6 and GO5 systems, with a reduction of approximately 14% in Na^+ and 13% in Cl^- rejection. These results are essential because they elucidate the potential for enhancing water permeability while maintaining salt rejection.

Although MD simulations are not meant to match experimental rejection values exactly, they remain important tools for clarifying the molecular mechanisms governing ion exclusion in GO nanochannels. Within the range of geometrical parameters explored here, variations in slit width, interlayer spacing, and commensurability strongly influence water permeability, while the impact on ion rejection remains comparatively small. This trend is consistent with experimental observations showing that GO modification leads to a significant increase in hydraulic permeability while maintaining salt rejection above 90%. Therefore, the simulations provide a mechanistic explanation for the experimental trend, indicating that geometrical rearrangements of the nanochannels can substantially enhance water transport without significantly altering the energetic barriers governing ion permeation.

https://doi.org/10.1021/acsanm.6c00110
ACS Appl. Nano Mater. 2026, 9, 7994−8008

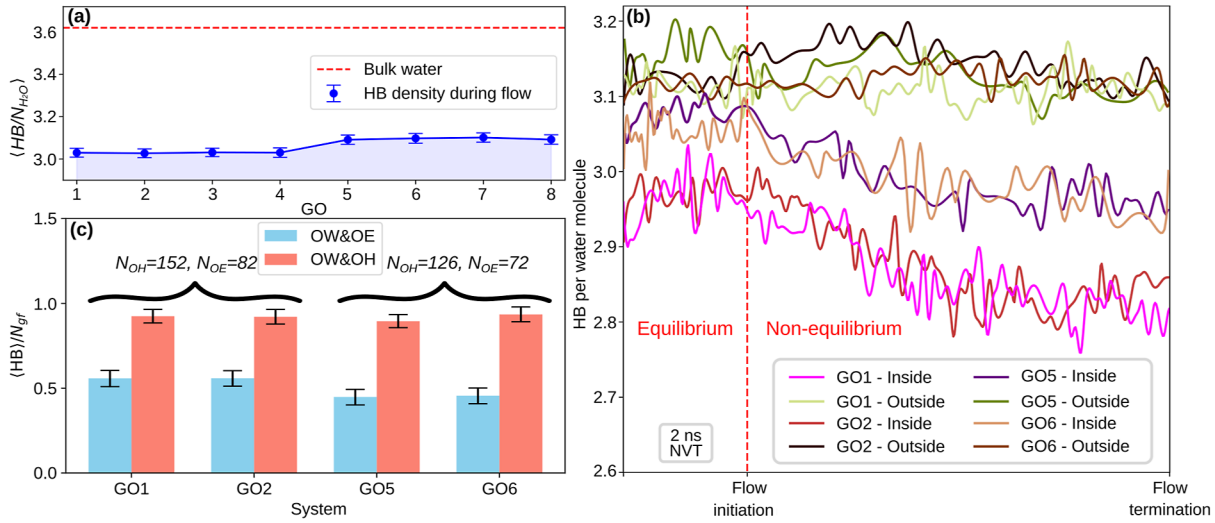

Figure 7. (a) The HB density of water for each system, (b) the HB density of water within the region occupied by the membranes and outside this region for the GO1−2 and GO5−6 systems, and (c) the number of HBs with functional groups for the GO1−2 and GO5−6 systems, respectively. Averages and standard deviations were obtained from five independent simulations.

While the differences in water permeability between 1.0 and 1.5 nm pores are clearly due to the larger area of entrance for water, the mechanism behind the differences in permeability when the pore size is the same but commensurability is varied remains unclear. To explore these distinctions, we analyze the colormaps in Figure 6.

Figure 6a,b show the water distribution in the *yz*-plane over the entire simulation for GO5 and GO6, respectively. Among all the available systems, these exhibit the most significant variations in permeability and salt rejection as commensurability is varied, while keeping the slit size and interlayer spacing fixed. Water distribution exhibits a smoothed transition between the slits in the GO6 system, whereas GO5 shows small regions of lower water distribution between adjacent slits. It indicates that the increase in commensurability promotes a more homogeneous water distribution, which explains the higher water permeability observed for GO6 in Figure 5b.

In both cases, as shown in Figure 6c,d, well-localized regions of higher water probability density on the *xy*-plane can be observed before, inside, and after the slits in each sheet. The distributions suggest that water organizes itself at specific sites to move from the feed to the permeate reservoir. In other words, water molecules may establish preferential pathways as they flow through the slits. In fact, Nair et al.[44] have shown that water molecules in lamellar-type membranes display permeation mainly based on the interlayer gallery pathways.

To gain deeper insights into its structural dynamics, we analyzed the HB network of the transported water molecules. These bonds are key to many of water's distinctive properties, driving a range of anomalies and playing a crucial role in various physical, chemical, and biological phenomena, including the formation and stability of numerous aqueous systems.[45−47]

In Figure 7a, we show the average HB density between water molecules, during the pressure-driven flow regime. Compared to the reference value for bulk water, approximately 3.6 HBs per water molecule[48−50] (red dashed line), all systems exhibit lower averages, which is expected given the presence of ions[51,52] and the formation of HBs between water and the functional groups on the graphene oxide layers[53] (see Figure 7c). These factors hinder the structuring of the water HB.

Figure 7a shows an increase in the number of HB density between systems with a 1.0 nm slit size (GO1−4) and those with a 1.5 nm slit size (GO5−8), which can be explained by the larger surface area of the graphene oxide membrane in the systems with narrower slits and, therefore, a larger number of functional groups. In addition, a decrease was observed in the number of HBs per water molecule inside the membrane region during the different time steps of the flow, with a stable count outside this region and before the flow (see Figure 7b). Although significant, this decrease does not continue indefinitely, reaching a stable behavior after approximately 40% of the total flow time. The confinement of the water flux can cause this geometric frustration through the channel created by the membranes.[54]

The implications of these results extend beyond the HB itself. In particular, the interaction of water with functional groups at the membrane surfaces may directly affect the mobility of molecules in different regions of the system. This connection becomes evident when analyzing the residence time correlation, which provides a quantitative measure of how long water remains confined near the membranes or within the slit regions.

The residence time correlation is the probability that water molecules initially within a delimited region remain in that region over time. Evaluating the correlation between water residence profiles and residence times is extremely important for understanding various properties and the behavior of water in complex systems, as well as for obtaining accurate information on water wettability, anomalous diffusion, interactions between water molecules and their surrounding environment, and the relationship between these metrics and the system's nonequilibrium dynamics.[55]

Figure 8a shows the different regions defined for the residence time correlation analysis, representing volumes encompassing the membranes (odd-numbered regions) and volumes within the slits (even-numbered regions). The regions were configured using the box limits along the *x* and *y*-axes, while the *z*-axis limits were adjusted to ensure equal volumes across all regions. For the systems with smaller slits, GO1 and GO2, Figure 8b,c, show that the residence time correlation exhibits a clear separation of decay rates between membrane

https://doi.org/10.1021/acsanm.6c00110
ACS Appl. Nano Mater. 2026, 9, 7994−8008

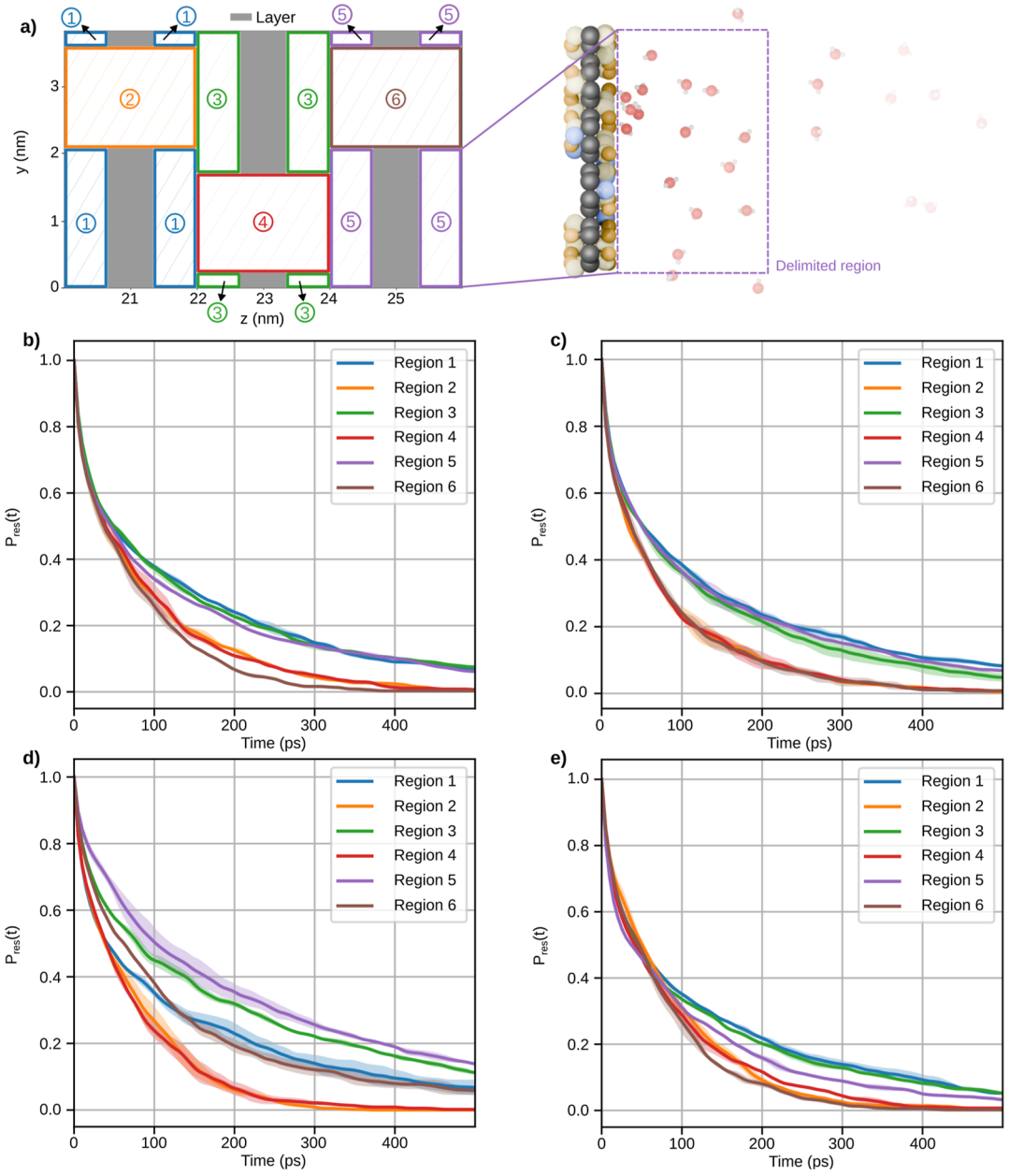

Figure 8. (a) Definition of regions for water residence time analysis. (b−e) Residence probability profiles for low-commensurability (GO1, GO5) and high-commensurability (GO2, GO6) systems. Shaded areas represent the standard deviation calculated from five independent data sets.

and slit regions. For the larger slits (GO5 and GO6), Figure 8d,e indicate a less clear distinction between the residence time of the different regions.

The fitted biexponential function

$$P_{res}(t) = Ae^{-t/\tau_1} + Be^{-t/\tau_2} \quad (2)$$

yields the corresponding residence times τ_1 and τ_2. For normalized profiles, $A + B = 1$, where A and B are the amplitudes associated with each decay regime.

Figure 9a,b illustrate the residence times τ_1 and τ_2, respectively, for the smaller slit configurations GO1 and GO2 for each one of the six regions shown in the Figure 8a. In this case, water molecules remain longer in membrane regions compared to slit regions, revealing a common spatial dependence of mobility. By comparing Figure 9a,b with 6c,d, we can see that longer residence times correspond to lower distribution of particles.

For systems with larger slits, GO5 and GO6 (Figure 8d,e), we observe a similar trend, with separation into two decay regimes. However, the curves for GO6 are closer together, suggesting greater variability across regions despite their shared spatial and structural characteristics. The residence times shown in Figure 9c,d confirm this trend, with both systems showing longer average retention in the membrane regions, but with higher differences in the mean values across similar regions. Interestingly, although GO5 and GO6 exhibit higher permeabilities than GO1 and GO2, their residence times are not systematically shorter. This apparent decoupling highlights the role of commensurability between the slit geometry and the water structure: enhanced transport may arise not from reduced local residence, but from improved connectivity and cooperative pathways across the channels. In all systems,

https://doi.org/10.1021/acsanm.6c00110
ACS Appl. Nano Mater. 2026, 9, 7994−8008

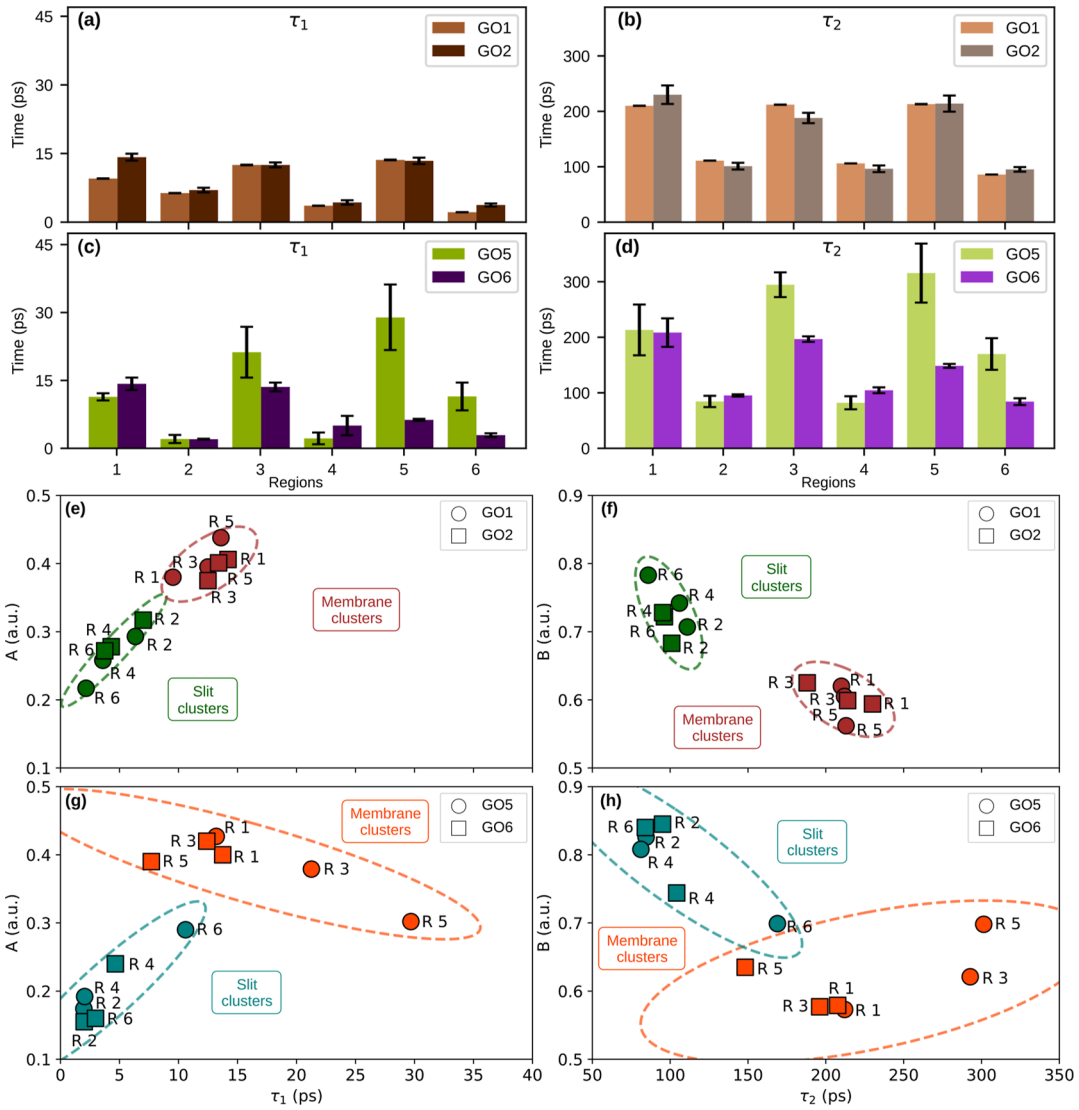

Figure 9. (a–d) Residence times for τ_1 and τ_2 decay regimes in GO1–2 and GO5–6 systems across regions defined in Figure 8a. (e–h) K-means clustering for GO1–2 (e,f) and GO5–6 (g,h) using parameters from both decay regimes. Error bars represent the standard deviation from five independent data sets.

hydrogen bonds formed between water and the functional groups on the graphene oxide layers, see Figure 7c, contribute to retaining water in the vicinity of the membranes, further explaining the consistently higher residence times in these regions.

In Figure 9e–h, we illustrate the grouping of regions in each system, based on their amplitudes and characteristic residence times in each decay regime, which govern the probability of water molecules remaining in each region. These groupings were obtained using the k-means algorithm, a clustering method based on the optimization of the sum of squared Euclidean distances from each point to the nearest centroid, thereby minimizing the internal variation within each cluster (for more information, see the section about k-means analysis in the Supporting Information). In this analysis, the algorithm was set to find two groups per system.

From a general standpoint, in both decay regimes shown in Figure 9e–h, k-means clustering consistently splits each system into two groups corresponding to the slit and membrane regions. These results confirm that common regional characteristics exert a similar influence on water-molecule displacement, regardless of commensurability. Although similar regions are well clustered in all available systems, thus confirming the regional separation, the clusters' compactness is significantly affected by the slit size. For the narrower slit systems with 1 nm, GO1 and GO2, the mean dispersion of the points from the centroid is notably lower (e.g., membrane cluster at the first decay regime: 1.11 ps^{-1} and slit cluster: 1.43 ps^{-1}; membrane cluster at the second decay regime: 8.11 ps^{-1} and slit cluster: 6.76 ps^{-1}), indicating that the residence time profiles for these systems, as shown in Figure 8b,c, within each group (slit or membrane) are highly homogeneous. In comparison, for the systems with wider 1.5 nm slit, GO5 and GO6, the mean dispersion is considerably increased (e.g., membrane cluster at the first decay regime: 6.10 ps^{-1} and slit cluster: 2.40 ps^{-1}; membrane cluster at the second decay regime: 47.15 ps^{-1} and slit cluster: 22.36 ps^{-1}). This higher dispersion, or lower compactness, suggests that although the k-means method correctly classifies the regions, there is greater heterogeneity in the decay parameters across different slits and membranes. These results are expected due to the greater

https://doi.org/10.1021/acsanm.6c00110
ACS Appl. Nano Mater. 2026, 9, 7994–8008

volume and, consequently, greater variation in water dynamics in the larger slits, reflected in a higher permeability.

The Taylor diagrams in Figures S3 and S4 of the Supporting Information present the Pearson correlation (corr), the centered root-mean-square (CRMS), and the standard deviation (σ) for each probability residence time profile across the GO1−2 and GO5−6 systems, respectively. The standard deviation reflects the variability of the curve values relative to their average, while the CRMS quantifies the difference in profile shape. From a general perspective, these diagrams consistently highlight the spatial dependence of water molecule dynamics, which is common to all systems. Strong correlations are observed among residence time probability profiles both within slit regions and among those associated with membrane regions. Importantly, the range of standard deviations is highly similar across the four systems—GO1 (0.167−0.191), GO2 (0.172−0.197), GO5 (0.173−0.197), and GO6 (0.172−0.209)—demonstrating comparable variability overall. The effect of the slit width is best observed by analyzing the CRMS and correlations between regions. The primary difference between the 1 nm slit size systems (GO1 and GO2) and the 1.5 nm systems (GO5 and GO6) lies in the degree of dynamic interdependence between the slit and membrane regions, as reflected by the CRMS. In the 1 nm slit systems, the strong confinement results in lower CRMS in the slit region than in the membrane region, indicating coupled dynamics and profiles with a more unified shape. For instance, the $CRMS_{R5,R2}$ (CRMS between regions 5 and 2) is 0.0253 for GO1 and 0.0278 for GO2. In wider slit systems, the larger spacing allows the dynamics within the slits to decouple more significantly from those on the membrane surfaces. This manifests as significantly higher CRMS values (a larger difference in profile shape) when comparing slit and membrane regions: the $CRMS_{R5,R2}$ is 0.0621 for GO5 (the highest among all systems) and 0.0410 for GO6. Regarding the correlation, the narrow slit systems maintain a robust correlation between slit and membrane regions (the minimum correlation is $corr_{R1,R6}$ = 0.9757 for GO1 and $corr_{R1,R4}$ = 0.9867 for GO2). However, the GO5 system exhibits the lowest correlation of all ($corr_{R5,R2}$ = 0.9449), which strongly suggests that the slit width increase, combined with poor commensurability, maximizes the dynamic decoupling. In contrast, the GO6 system exhibits higher correlations between slit and membrane regions (the minimum correlation is $corr_{R1,R2}$ = 0.9870), demonstrating that commensurability acts as a structural key factor, mitigating the decoupling effect of slit enlargement and maintaining a strong similarity in the behavior of the residence time profiles across regions. In fact, the flow magnitude is predominantly governed by the slit width. When moving from 1 to 1.5 nm, the lowest increase in mean permeability is approximately 97.85 ns^{-1}, which is around three times larger than the maximum difference observed among any 1 nm systems. These results are consistent with the greater available volume and the increased dispersion of the k-means clusters observed for GO5 and GO6, indicating a higher volume of water with less confined, faster dynamics in the larger slits, thereby boosting the overall flow rate. Within each slit width, the high commensurability significantly increases permeability compared to the systems with lower commensurability. From GO1 to GO2, commensurability increases the permeability by approximately 12%, whereas from GO5 to GO6, the increase is approximately 25%. This gain in permeability is intimately connected to the homogeneity and dynamic coupling quantified in the Taylor analysis. The local behavior is also more expressive in wider slit systems. Although GO5 has a wider slit, its permeability is significantly lower than that of GO6 due to its greater dynamic heterogeneity. The higher correlation values and the lower CRMS between slit and membrane regions observed in the GO6 system, relative to GO5, indicate that the decoordination of water molecules during flow, caused by the slit enlargement, is diminished by the increase in commensurability. In other words, dynamic bottlenecks that act as critical points with high resistance to flow, thereby strangling the global flow and decoupling the slit-membrane dynamics, are mitigated by increased commensurability.

3.3. Combining Experimental and Simulation Results

The theoretical results reveal that subtle variations in nanoscale confinement, such as slit width, interlayer spacing, and commensurability between adjacent slits, significantly influence water structuring, hydrogen-bond dynamics, and residence-time distributions within the confined regions. These effects, which cannot be individually controlled in the experimental module, help explain how preferential flow pathways emerge and how specific structural arrangements can either amplify or hinder water transport. The observed relationship between increased commensurability and enhanced permeability supports the idea that aligned GO regions, similar to those formed along the spacer-induced grooves seen experimentally, can act as high-flux domains.

Furthermore, the simulations show that increasing the slit width and interlayer spacing yields substantial gains in water permeability while maintaining ion rejection, a behavior entirely consistent with the experimental findings. The formation of extended low-friction pathways, combined with hydration-shell exclusion for ions, constitutes a fundamental mechanism underlying this trend. As such, the theoretical analysis provides a clear molecular-level explanation for the approximately 25% increase in hydraulic permeability observed in the GO-modified membrane.

Finally, the evaluation of hydrogen bond networks and residence time clustering indicates that GO surfaces promote regions of reduced confinement and enhanced water mobility, reinforcing the "frictionless channel" hypothesis frequently invoked in the literature. Specifically, the transition from 1.0 to 1.5 nm slits yields a substantial increase in the maximum average flow rate, rising from approximately 160 ns^{-1} (GO4) to 380 ns^{-1} (GO8). This improvement in permeability is directly correlated with the HB network environment; systems with wider slits exhibit a higher water−water HB density (∼3.1) compared to narrower channels (∼3.03), where the higher surface-to-volume ratio and number of functional groups hinder HB restructuring. Although subtle, this difference in HB density is reproducible and consistent across systems with 1.0 and 1.5 nm slits. Furthermore, the clustering analysis based on second-regime residence times confirms that higher permeability is not merely a product of shorter local stays, but of changes in dynamic coupling. Systems with narrower slits exhibit high compactness and homogeneity, characterized by a dispersion of 6.76 ps^{-1} and an intercluster distance of 112 ps^{-1}. In contrast, wider-slit clusters exhibit lower compactness, with a dispersion of 22.36 ps^{-1} and a separation of 123.3 ps^{-1}, reflecting a higher degree of heterogeneity in local water dynamics that translates directly into enhanced macroscopic permeability. The combination of

https://doi.org/10.1021/acsanm.6c00110
ACS Appl. Nano Mater. 2026, 9, 7994−8008

GO-induced structural alignment, surface smoothing, and altered water organization at the GO−polyamide interface suggests that the observed superflow likely arises from a collective, synergistic effect rather than a single isolated mechanism. In this way, integrating experimental evidence with theoretical modeling yields a coherent, comprehensive picture of GO's role in water transport, providing a solid foundation for the rational design of next-generation high-performance desalination membranes.

4. CONCLUSIONS

In this paper, we analyze the permeability of water and the rejection of salt when using a desalination membrane. Our assumption is that the GO membrane allows water to be structured, which enhances permeability, while polymeric membranes, such as pristine polyamide, promote disorganization, particularly at high pressures, thereby decreasing permeability.

First, this assumption is tested experimentally using both a pure polymeric membrane and a membrane covered by GO. The experimental findings demonstrate that the incorporation of GO onto commercial polyamide membranes produces three key effects: (i) a clear modification of the surface morphology, with GO preferentially accumulating along the spacer-imprinted grooves; (ii) a substantial reduction in surface roughness, resulting in a smoother and more uniform topography; and (iii) a marked enhancement of hydraulic permeability of approximately 25%, while salt rejection remains above 90%. These observations confirm that GO effectively reorganizes the membrane surface without compromising its selective polyamide layer, enabling fast water transport through regions of reduced friction and improved hydrophilicity.

The theoretical and MD analyses further reveal that water mobility within GO-based nanochannels is highly sensitive to geometric parameters, including slit width, interlayer spacing, and commensurability between adjacent slits. Wider slits and larger interlayer distances increase the available free volume and accelerate transport, while high commensurability promotes dynamic coupling across similar regions, suppresses bottlenecks, and enhances global water flux. The MD simulations also show that water molecules develop preferential pathways, undergo significant network destructuring within the membrane region, and experience strong spatial dependence of residence times, all signatures of complex nanoscale transport behavior modulated by GO morphology.

Considering that the theoretical framework focuses on idealized representations of the experimental setup, it is notable that both experimental and theoretical results converge toward a unified mechanistic picture. The experimentally observed enhancement in membrane permeability is closely aligned with the molecular-scale mechanisms revealed in the simulations: low-friction pathways forming between GO sheets, structural alignment that improves connectivity between channels, and modified hydrogen-bond environments that facilitate rapid water mobility. This synergy provides a comprehensive explanation for how GO modifies transport pathways without compromising ionic exclusion. Beyond elucidating the mechanisms underlying the observed superflow, these combined results establish a solid framework for the rational design of next-generation desalination membranes in which nanoscale geometry and macroscopic performance are jointly optimized. These findings refine the integration of GO membranes into commercial polyamide modules, enhancing both their understanding and practical application.

■ ASSOCIATED CONTENT

Data Availability Statement

The data underlying this study are available in the published article and its Supporting Information. Any additional data is available from the corresponding author upon reasonable request.

Supporting Information

The Supporting Information is available free of charge at https://pubs.acs.org/doi/10.1021/acsanm.6c00110.

Containing information regarding the water flux through the graphene oxide membranes, ionic density profiles, color maps, and Taylor diagrams (PDF)

■ AUTHOR INFORMATION

Corresponding Authors

Marcia C. Barbosa − *Instituto de Física, Universidade Federal do Rio Grande do Sul, Porto Alegre 91501-970, Brazil;* orcid.org/0000-0001-5663-6102; Email: marcia.barbosa@ufrgs.br

Mateus H. Köhler − *Departamento de Física, Universidade Federal de Santa Maria, Santa Maria 97105-900, Brazil;* orcid.org/0000-0001-9733-9630; Email: mateus.kohler@ufsm.br

Authors

Yan A. S. da Campo − *Departamento de Física, Universidade Federal de Santa Maria, Santa Maria 97105-900, Brazil;* orcid.org/0000-0002-5408-5877

Ezequiel Lorenzett − *Instituto de Química, Universidade Federal do Rio Grande do Sul, Porto Alegre 91501-970, Brazil*

Paulo A. Netz − *Instituto de Química, Universidade Federal do Rio Grande do Sul, Porto Alegre 91501-970, Brazil;* orcid.org/0000-0003-4242-0591

Marcelo L. Pereira Junior − *College of Technology, Department of Electrical Engineering, University of Brasília, Brasília, Federal District 70910-900, Brazil; Department of Materials Science and NanoEngineering, Rice University, Houston, Texas 77005, United States;* orcid.org/0000-0001-9058-510X

Claudia K. B. de Vasconcelos − *CTNano-Centro de Tecnologia em Nanomateriais e Grafeno, Departamento de Química, Universidade Federal de Minas Gerais, Belo Horizonte 31270-901, Brazil*

Glaura G. Silva − *CTNano-Centro de Tecnologia em Nanomateriais e Grafeno, Departamento de Química, Universidade Federal de Minas Gerais, Belo Horizonte 31270-901, Brazil*

Complete contact information is available at: https://pubs.acs.org/10.1021/acsanm.6c00110

Funding

The Article Processing Charge for the publication of this research was funded by the Coordenacao de Aperfeicoamento de Pessoal de Nivel Superior (CAPES), Brazil (ROR identifier: 00x0ma614).

Notes

The authors declare no competing financial interest.

■ ACKNOWLEDGMENTS

The authors thank Petrobras, Minas Gerais Research Support Foundation (FAPEMIG), National Council for Scientific and Technological Development (CNPq), and the Center of Microscopy at the Federal University of Minas Gerais (http://www.microscopia.ufmg.br) for providing the equipment and technical support for experiments involving electron microscopy. The authors also acknowledge the CPAD-UFSM and CENAPAD-SP for the computational time. M.L.P.J. acknowledges financial support from FAPDF (grant 00193-00001807/2023-16) and CAPES (grant 88887.005164/2024-00). M.C.B. and M.H.K. thank CNPq for the Universal grant No. 405479/2023-9. M.H.K., M.L.P.J., and P.A.N. acknowledge financial support from CNPq grants 303649/2024-0, 444921/2024-9, and 307106/2021-7, respectively. This work was carried out with the support of the Coordination for the Improvement of Higher Education Personnel—Brazil (CAPES)—Financing Code 001.

■ REFERENCES

(1) Veldkamp, T.; Wada, Y.; Aerts, J.; Döll, P.; Gosling, S. N.; Liu, J.; Masaki, Y.; Oki, T.; Ostberg, S.; Pokhrel, Y.; et al. others Water scarcity hotspots travel downstream due to human interventions in the 20th and 21st century. *Nat. Commun.* **2017**, *8*, 15697.

(2) Mekonnen, M. M.; Hoekstra, A. Y. Four billion people facing severe water scarcity. *Sci. Adv.* **2016**, *2*, No. e1500323.

(3) Jones, E.; Qadir, M.; van Vliet, M. T.; Smakhtin, V.; Kang, S.-m. The state of desalination and brine production: A global outlook. *Sci. Total Environ.* **2019**, *657*, 1343−1356.

(4) Uhlenbrook, S.; Connor, R. *Others the United Nations World Water Development Report 2019: Leaving No One Behind*; UNESCO, 2019; Vol. *7*, pp 1−201.

(5) Elimelech, M.; Phillip, W. A. The future of seawater desalination: energy, technology, and the environment. *Science* **2011**, *333*, 712−717.

(6) Khorshidi, B.; Thundat, T.; Fleck, B. A.; Sadrzadeh, M. A novel approach toward fabrication of high performance thin film composite polyamide membranes. *Sci. Rep.* **2016**, *6*, 22069.

(7) Kucera, J. Biofouling of polyamide membranes: Fouling mechanisms, current mitigation and cleaning strategies, and future prospects. *Membranes* **2019**, *9*, 111.

(8) Boretti, A.; Al-Zubaidy, S.; Vaclavikova, M.; Al-Abri, M.; Castelletto, S.; Mikhalovsky, S. Outlook for graphene-based desalination membranes. *npj Clean Water* **2018**, *1*, 5.

(9) Heiranian, M.; Farimani, A. B.; Aluru, N. R. Water desalination with a single-layer MoS2 nanopore. *Nat. Commun.* **2015**, *6*, 8616.

(10) Köhler, M. H.; Bordin, J. R.; de Matos, C. F.; Barbosa, M. C. Water in nanotubes: The surface effect. *Chem. Eng. Sci.* **2019**, *203*, 54−67.

(11) Dehaghani, M. Z.; Mashhadzadeh, A. H.; Vafa, N.; Firoozabadi, B.; Nouranian, S.; Golman, B.; Spitas, C. Evaluation of water desalination performances of functionalized nanoporous graphene membranes by molecular dynamics simulation. *Comput. Mater. Sci.* **2023**, *228*, 112308.

(12) Liu, Q.; Xu, G.-R. Graphene oxide (GO) as functional material in tailoring polyamide thin film composite (PA-TFC) reverse osmosis (RO) membranes. *Desalination* **2016**, *394*, 162−175.

(13) Cohen-Tanugi, D.; Grossman, J. C. Water desalination across nanoporous graphene. *Nano Lett.* **2012**, *12*, 3602−3608.

(14) Wei, N.; Peng, X.; Xu, Z. Understanding water permeation in graphene oxide membranes. *ACS Appl. Mater. Interfaces* **2014**, *6*, 5877−5883.

(15) Chen, B.; Jiang, H.; Liu, X.; Hu, X. Molecular Insight into Water Desalination across Multilayer Graphene Oxide Membranes. *ACS Appl. Mater. Interfaces* **2017**, *9*, 22826−22836.

(16) Lorenzett, E.; da Campo, Y. A. S.; Loubet, N. A.; Appignanesi, G. A.; Netz, P. A.; Köhler, M. H. Role of Oxidation and Confinement Level in Water Trapping between Graphene and Graphene Oxide. *J. Phys. Chem. C* **2026**, *130* (16), 5979−5994.

(17) Bordin, J. R.; Diehl, A.; Barbosa, M. C. Relation between flow enhancement factor and structure for core-softened fluids inside nanotubes. *J. Phys. Chem. B* **2013**, *117*, 7047−7056.

(18) Abal, J. P. K.; Barbosa, M. C. Molecular fluid flow in MoS2 nanoporous membranes and hydrodynamics interactions. *J. Chem. Phys.* **2021**, *154*, 134506.

(19) Oliveira, C.; dos Santos, R.; Viegas, J.; Souza, R.; Silva, R.; Pinto, H.; Viana, M.; Amaral, M.; de Vasconcelos, C.; Silva, G. In situ graphene oxide surface modification of spiral-wound RO membranes for enhanced chlorine resistance and antifouling performance. *J. Water Process Eng.* **2025**, *79*, 109060.

(20) de Oliveira, C. P. M.; Viana, M. M.; Silva, G. R.; Frade Lima, L. S.; Coutinho de Paula, E.; Amaral, M. C. S. Potential use of green TiO2 and recycled membrane in a photocatalytic membrane reactor for oil refinery wastewater polishing. *J. Clean. Prod.* **2020**, *257*, 120526.

(21) Shao, F.; Su, X.; Shen, X.; Ren, S.; Wang, H.; Yi, Z.; Xu, C.; Yu, L.; Dong, L. Highly improved chlorine resistance of polyamide reverse membrane by grafting layers of graphene oxide. *Sep. Purif. Technol.* **2021**, *254*, 117586.

(22) Thompson, A. P.; Aktulga, H. M.; Berger, R.; Bolintineanu, D. S.; Brown, W. M.; Crozier, P. S.; in 't Veld, P. J.; Kohlmeyer, A.; Moore, S. G.; Nguyen, T. D.; Shan, R.; Stevens, M. J.; Tranchida, J.; Trott, C.; Plimpton, S. J. LAMMPS - a flexible simulation tool for particle-based materials modeling at the atomic, meso, and continuum scales. *Comput. Phys. Commun.* **2022**, *271*, 108171.

(23) Wang, Y.; He, Z.; Gupta, K. M.; Shi, Q.; Lu, R. Molecular dynamics study on water desalination through functionalized nanoporous graphene. *Carbon* **2017**, *116*, 120−127.

(24) Shen, J.-W.; Li, J.; Liu, F.; Zhang, L.; Liang, L.; Wang, H.; Wu, J.-Y. A molecular dynamics study on water desalination using single-layer MoSe2 nanopore. *J. Membr. Sci.* **2020**, *595*, 117611.

(25) Ferreira, R. M. S.; Abal, J. P. K.; Côrtes, P. R. B.; Pereira, M. L. J.; Köhler, M. H.; Netz, P. A.; Barbosa, M. C. Performance comparison of slit and nanoporous graphene oxide membranes in water desalination. *J. Chem. Phys.* **2026**, *164*, 054501.

(26) Hosseini, M.; Azamat, J.; Erfan-Niya, H. Improving the performance of water desalination through ultra-permeable functionalized nanoporous graphene oxide membrane. *Appl. Surf. Sci.* **2018**, *427*, 1000−1008.

(27) Berendsen, H.-J.-C.; Grigera, J.-R.; Straatsma, T. P. The missing term in effective pair potentials. *J. Phys. Chem.* **1987**, *91*, 6269−6271.

(28) Ryckaert, J.-P.; Ciccotti, G.; Berendsen, H. J. Numerical Integration of the Cartesian Equations of Motion of a System with Constraints: Molecular Dynamics of n-Alkanes. *J. Comput. Phys.* **1977**, *23*, 327−341.

(29) Nosé, S. A Molecular Dynamics Method for Simulations in the Canonical Ensemble. *Mol. Phys.* **1984**, *52*, 255.

(30) Perreault, F.; Tousley, M. E.; Elimelech, M. Thin-film composite polyamide membranes functionalized with biocidal graphene oxide nanosheets. *Environ. Sci. Technol. Lett.* **2014**, *1*, 71−76.

(31) Souza, M. L. d.; Moscardini, S. B.; Faria, E. H. d.; Ciuffi, K. J.; Rocha, L. A.; Nassar, E. J.; Silva, J. V.; Oliveira, M. F.; Maia, I. A. Óxido de ítrio e aluminio dopado com Yb3+ e Er3+ incorporado em membrana de poliamida. *Química Nova* **2018**, *41*, 519−527.

(32) Deimede, V.; Voyiatzis, G.; Kallitsis, J.; Qingfeng, L.; Bjerrum, N. Miscibility behavior of polybenzimidazole/sulfonated polysulfone blends for use in fuel cell applications. *Macromolecules* **2000**, *33*, 7609−7617.

(33) Xia, S.; Yao, L.; Zhao, Y.; Li, N.; Zheng, Y. Preparation of graphene oxide modified polyamide thin film composite membranes

https://doi.org/10.1021/acsanm.6c00110
ACS Appl. Nano Mater. 2026, 9, 7994−8008

with improved hydrophilicity for natural organic matter removal. *Chem. Eng. J.* **2015**, *280*, 720−727.
(34) Cho, Y. H.; Han, J.; Han, S.; Guiver, M. D.; Park, H. B. Polyamide thin-film composite membranes based on carboxylated polysulfone microporous support membranes for forward osmosis. *J. Membr. Sci.* **2013**, *445*, 220−227.
(35) Han, G.; Zhang, S.; Li, X.; Widjojo, N.; Chung, T.-S. Thin film composite forward osmosis membranes based on polydopamine modified polysulfone substrates with enhancements in both water flux and salt rejection. *Chem. Eng. Sci.* **2012**, *80*, 219−231.
(36) Salahshoori, I.; Seyfaee, A.; Babapoor, A. Recent advances in synthesis and applications of mixed matrix membranes. *Synth. Sinter.* **2021**, *1*, 1−27.
(37) Croll, H.; Soroush, A.; Pillsbury, M. E.; Romero-Vargas Castrillón, S. Graphene oxide surface modification of polyamide reverse osmosis membranes for improved N-nitrosodimethylamine (NDMA) removal. *Sep. Purif. Technol.* **2019**, *210*, 973−980.
(38) Castelletto, S.; Boretti, A. Advantages, limitations, and future suggestions in studying graphene-based desalination membranes. *RSC Adv.* **2021**, *11*, 7981−8002.
(39) Bhoje, R.; Ghosh, A. K.; Nemade, P. R. Development of performance-enhanced graphene oxide-based nanostructured thin-film composite seawater reverse osmosis membranes. *ACS Appl. Polym. Mater.* **2022**, *4*, 2149−2159.
(40) Köhler, M. H.; Bordin, J. R.; Barbosa, M. C. 2D nanoporous membrane for cation removal from water: Effects of ionic valence, membrane hydrophobicity, and pore size. *J. Chem. Phys.* **2018**, *148*, 222804.
(41) Zhou, J.; Lu, X.; Wang, Y.; Shi, J. Molecular dynamics study on ionic hydration. *Fluid Phase Equilib.* **2002**, *194−197*, 257−270.
(42) Chen, C.; Zhang, L. Effects of structural parameters on the desalination performance of a multilayer stacked graphene oxide membrane: insights from molecular dynamics simulation. *Nanoscale* **2025**, *17*, 12868−12879.
(43) Alinia, Z.; Akbarzadeh, H.; Mohammadi Zonoz, F.; Tayebee, R. Enhancing the seawater desalination performance of multilayer reduced graphene oxide membranes by introducing in-plane nanopores: a molecular dynamics simulation study. *Phys. Chem. Chem. Phys.* **2024**, *26*, 9722−9732.
(44) Nair, R. R.; Wu, H. A.; Jayaram, P. N.; Grigorieva, I. V.; Geim, A. K. Unimpeded Permeation of Water Through Helium-Leak−Tight Graphene-Based Membranes. *Science* **2012**, *335*, 442−444.
(45) Djikaev, Y.; Ruckenstein, E. The variation of the number of hydrogen bonds per water molecule in the vicinity of a hydrophobic surface and its effect on hydrophobic interactions. *Curr. Opin. Colloid Interface Sci.* **2011**, *16*, 272−284.
(46) Reid, K. M.; Poudel, H.; Leitner, D. M. Dynamics of Hydrogen Bonds between Water and Intrinsically Disordered and Structured Regions of Proteins. *J. Phys. Chem. B* **2023**, *127*, 7839−7847.
(47) Hou, Y.; Wang, M.; Chen, X.; Hou, X. Continuous water-water hydrogen bonding network across the rim of carbon nanotubes facilitating water transport for desalination. *Nano Res.* **2021**, *14*, 2171−2178.
(48) Thompson, H.; Soper, A. K.; Ricci, M. A.; Bruni, F.; Skipper, N. T. The Three-Dimensional Structure of Water Confined in Nanoporous Vycor Glass. *J. Phys. Chem. B* **2007**, *111*, 5610−5620.
(49) Chava, B. S.; Das, S. Strength, number, and kinetics of hydrogen bonds for water confined inside boron nitride nanotubes. *Nanoscale Adv.* **2024**, *6*, 3329−3337.
(50) Kumar, R.; Schmidt, J. R.; Skinner, J. L. Hydrogen bonding definitions and dynamics in liquid water. *J. Chem. Phys.* **2007**, *126*, 204107.
(51) Di Lecce, S.; Albrecht, T.; Bresme, F. Taming the thermodiffusion of alkali halide solutions in silica nanopores. *Nanoscale* **2020**, *12*, 23626−23635.
(52) Thomas, A. S.; Elcock, A. H. Molecular Dynamics Simulations of Hydrophobic Associations in Aqueous Salt Solutions Indicate a Connection between Water Hydrogen Bonding and the Hofmeister Effect. *J. Am. Chem. Soc.* **2007**, *129*, 14887−14898.
(53) Sun, C.; Zhou, R.; Zhao, Z.; Bai, B. Unveiling the hydroxyl-dependent viscosity of water in graphene oxide nanochannels via molecular dynamics simulations. *Chem. Phys. Lett.* **2021**, *778*, 138808.
(54) Abal, J. P. K.; Dillenburg, R. F.; Köhler, M. H.; Barbosa, M. C. Molecular Dynamics Simulations of Water Anchored in Multilayered Nanoporous MoS2Membranes: Implications for Desalination. *ACS Appl. Nano Mater.* **2021**, *4*, 10467−10476.
(55) Netz, P. A.; Dorfmüller, T. Computer Simulation Studies on the Polymer-Induced Modification of Water Properties in Polyacrylamide Hydrogels. *J. Phys. Chem. B* **1998**, *102*, 4875−4886.

https://doi.org/10.1021/acsanm.6c00110
ACS Appl. Nano Mater. 2026, 9, 7994−8008